SCIENCE CHINA
Physics, Mechanics & Astronomy

• Article •

October 2026 Vol. 69 No. 10: 104211
https://doi.org/10.1007/s11433-026-3032-6

High-gain multiband metasurface antennas driven by bound states in the continuum for extended millimeter-wave communications

Zhenxiong Li[1], Zhihui He[1*], Yashan Huo[1*], Xiongxiong Wu[1], Wei Cui[1], Zhimin Yang[1], Ye Zhao[1], Lei Zhang[1], Shasha Liang[1], Zhaoyang Liu[1], Kaiyan Xu[1], Zhancheng Li[2], and Shuqi Chen[2*]

[1] *The Key Laboratory of Advanced Optoelectronic Materials and Devices of Higher Education Institutions in Shaanxi, School of Physics and Electronic Information, Yan'an University, Yan'an 716000, China*

[2] *Key Laboratory of Weak-Light Nonlinear Photonics, Ministry of Education, School of Physics and TEDA Institute of Applied Physics, Nankai University, Tianjin 300071, China*

Received January 30, 2026; accepted May 29, 2026; published online August 26, 2026

The stringent requirements for ultrahigh gain, programmable beamforming, and multiband coexistence in 5G/6G extended millimeter-wave communications are fundamentally constrained by the intrinsic bandwidth-gain trade-off of conventional metasurface antennas. Here, we propose a metasurface antenna that integrates bound states in the continuum (BICs) with aperture coupling to improve field confinement, radiation control, and impedance matching. By exploiting symmetry-protected and quasi-BIC resonances with suppressed radiation leakage, the proposed architecture enables selective resonance excitation and controllable energy localization across 20-42 GHz. Through geometric optimization of quasi-BIC meta-atoms and parametric tuning of coupling apertures, the radiating metasurface achieves an ultrahigh Q-factor of 2.1×10^6, yielding a simulated peak gain of 22.4 dBi at 25.7 GHz and a maximum measured gain of 18.1 dBi, together with significantly improved return-loss performance compared with conventional designs. The results show that the combination of symmetrical perturbation and aperture-mediated coupling provides an effective route to balancing gain, frequency selectivity, and multiband operation. This work offers a promising strategy for high-efficiency and frequency-agile antennas in future wireless communication and sensing systems.

BIC metasurfaces, high *Q*-factors, extended millimeter-wave communications, high gain antenna

Citation: Z. Li, Z. He, Y. Huo, X. Wu, W. Cui, Z. Yang, Y. Zhao, L. Zhang, S. Liang, Z. Liu, K. Xu, Z. Li, and S. Chen, High-gain multiband metasurface antennas driven by bound states in the continuum for extended millimeter-wave communications, Sci. China-Phys. Mech. Astron. **69**, 104211 (2026), https://doi.org/10.1007/s11433-026-3032-6

1 Introduction

With the rapid development of sixth-generation (6G) wireless technologies, communication systems are evolving toward higher carrier frequencies, lower latency, and increased connectivity capacity [1]. Operating in the millimeter-wave and terahertz bands, 6G networks are expected to provide ultra-high data rates while imposing stringent system-level requirements on antennas, including high gain, high efficiency, programmable beamforming, wide-angle incidence adaptability, and multi-mode/multi-band coexistence [2-7]. These demands pose significant challenges to conventional antenna architectures, particularly under the constraints of limited spectrum resources and increasingly stringent

*Corresponding authors (Zhihui He, email: hezh@yau.edu.cn; Yashan Huo, email: huoyashan@yau.edu.cn; Shuqi Chen, email: schen@nankai.edu.cn)

frequency requirements. Metasurface antennas, enabled by artificially engineered sub-wavelength structures, offer dynamic control over electromagnetic (EM) wave propagation, reflection, and radiation patterns, thereby providing an attractive pathway to overcome these challenges [4,8-11]. Diverse metasurface antennas have been proposed to exploit sub-wavelength engineering for enhanced wavefront manipulation and advanced functionalities. For instance, the universal metasurface antenna (UMA), based on PIN-diode anisotropic meta-atoms integrated with space-time coding (STC), achieves comprehensive control of EM properties and provides enhanced physical-layer security through its directionally modulated radiation [12-16]. Similarly, a newly proposed dual-polarized reconfigurable metasurface antenna employing tunable resistors enables functionalities such as dual and quad-beam generation and radar cross-section (RCS) reduction [17-20]. These innovations highlight the broad potential of metasurface antennas in 5G/6G communications, quantum information, cognitive sensing, and imaging systems.

BICs are non-radiative resonances in open systems that exhibit ultrahigh quality factors (Q-factors) and strong field enhancement [21-27]. In metasurfaces, BICs give rise to ultra-narrowband, high-energy-storage resonant modes, forming an ideal physical platform for coupling between radiating apertures and resonant cavities. Owing to these properties, BIC metasurfaces have demonstrated compelling potential in high-sensitivity sensors, narrowband filters, and efficient photonic devices [28-32]. Furthermore, the topological features of BICs, such as polarization vortices and topological charges, introduce additional degrees of freedom in beam shaping, polarization manipulation, and directional control [33-38]. Compared with conventional metasurface approaches, BIC-enabled designs can exploit symmetry-protected and accidental BICs to achieve controllable mode excitation and tunable radiation characteristics [39-41]. By further integrating chiral metasurfaces and exploiting symmetry breaking as well as spin-dependent light-matter interactions, such designs facilitate ultrahigh-Q resonances, strong chiroptical responses, and controllable directional photonic routing [39,42-44]. Their ultrahigh Q-factors and negligible radiation losses suppress spurious emission, enhance fundamental-mode coupling efficiency, and enable highly directive radiation within extremely narrow bandwidths [45-48]. Nevertheless, the inherently strong field confinement of BICs restricts efficient energy transfer to external feeding systems, thereby impeding the concurrent realization of ultrahigh Q-factors and broadband radiation performance.

Aperture coupling serves as an efficient feeding mechanism, transferring energy from the excitation source to the radiating aperture via engineered slots. The geometric and spatial parameters of these slots can be optimized to balance radiation leakage and coupling efficiency [49-52]. However, this technique represents a typical resonant-type energy transfer mechanism, whose coupling efficiency is highly sensitive to frequency. In the millimeter-wave and terahertz bands, pronounced ohmic and dielectric absorption losses reduce energy transmission efficiency, making it challenging to simultaneously achieve broadband response and high-gain performance [53-56]. To overcome these limitations, BIC metasurfaces, characterized by ultrahigh Q-factors and strong EM field confinement, can effectively suppress both radiation and dissipative losses. Moreover, introducing symmetric breaking or geometric perturbations transforms an ideal BIC into a quasi-BIC that retains its high Q-factor while allowing a controllable radiation channel. While BICs-inspired resonances have already been explored in metasurfaces and antenna-related structures at microwave and millimeter-wave frequencies, their practical integration into compact, aperture-fed, finite-size radiating platforms remains challenging, especially when broadband impedance matching and high gain are simultaneously required.

Here, we propose an aperture-coupled BIC metasurface antenna that provides an effective approach to balancing gain and bandwidth in extended millimeter-wave communication systems while enabling multiband beam control. This work achieves tunable quasi-BIC resonances with a high Q-factor of up to 2.10×10^6 by tailoring the geometric parameters of the metasurface and breaking its in-plane structural symmetry, exhibiting exceptional EM manipulation capabilities. By integrating the aperture-coupling feeding technique with precisely engineered coupling apertures, the proposed design significantly improves impedance matching and radiation efficiency. Experimental results verify the directional radiation and multiband response of the proposed antenna, while the simulated peak gain reaches 22.4 dBi and the maximum measured gain is 18.1 dBi, validating the effectiveness of the BIC-enabled metasurface architecture. More importantly, by synergistically combining the high Q-factor confinement of BICs with the controllable energy leakage of aperture coupling, the proposed metasurface antenna achieves multiple resonant modes across the extended millimeter-wave band, with an overall bandwidth exceeding 50%. This work provides a unified physical framework for combining high-Q-factor confinement with aperture-mediated radiation and offers a feasible route toward high-efficiency and reconfigurable antenna architectures in the millimeter-wave and terahertz regimes.

2 Results and discussion

2.1 Symmetry-protected BIC metasurface model

We utilize symmetric metal surface structures and dielectric substrates to form BIC meta-atoms. By breaking the structural symmetry, radiation channels are introduced, allowing coupling to the incident wave and converting ideal BIC modes into quasi-BIC modes. The BIC metasurface consists of a Tly-5 substrate and periodically arranged Cu meta-atoms, each formed by four symmetric elliptical metal elements. The Tly-5 substrate, with a refractive index of 2.2+0.0009i, serves to reduce dielectric losses in the BICs. The lattice period along the x and y direction are p_x=p_y=5 mm, and the major and minor semi-axes of the Cu ellipses are a_t=1.2 mm and b_t=0.6 mm, respectively, as shown in Figure 1(a). Numerical simulations of the BIC metasurfaces are conducted using the finite element method (FEM) in Comsol Multiphysics. The boundary conditions are set as periodic in the x and y planes, with perfect matching layers applied along the z-direction. For clarity, metasurfaces supporting parameter-tuned BICs are referred to as PT metasurfaces, while metasurfaces supporting symmetry-protected BICs are called SP metasurfaces. Symmetry breaking is introduced by tuning the size (Δt) and rotation angle (θ) of one elliptical resonator while fixing the Tly-5 substrate thickness at 0.762 mm. This perturbation opens radiation channels and enables the incident wave to couple to the quasi-BIC modes, as illustrated in Figure 1(a). The asymmetry coefficient is defined as: $\alpha_1=(S-\Delta S)/S$ (S=4p×$a_t\times b_t$, ΔS=4p×$(a_t-\Delta t)\times(b_t-\Delta t)$), $\alpha_2=\theta/180°$. The BIC modes, which are fully confined within the radiation continuum, manifest as dark states. Their transmission spectra are represented by the black dotted lines in Figure 1(d)-(g). In contrast, the quasi-BIC modes exhibit partial energy radiation, as indicated by the red lines, displaying ultranarrow

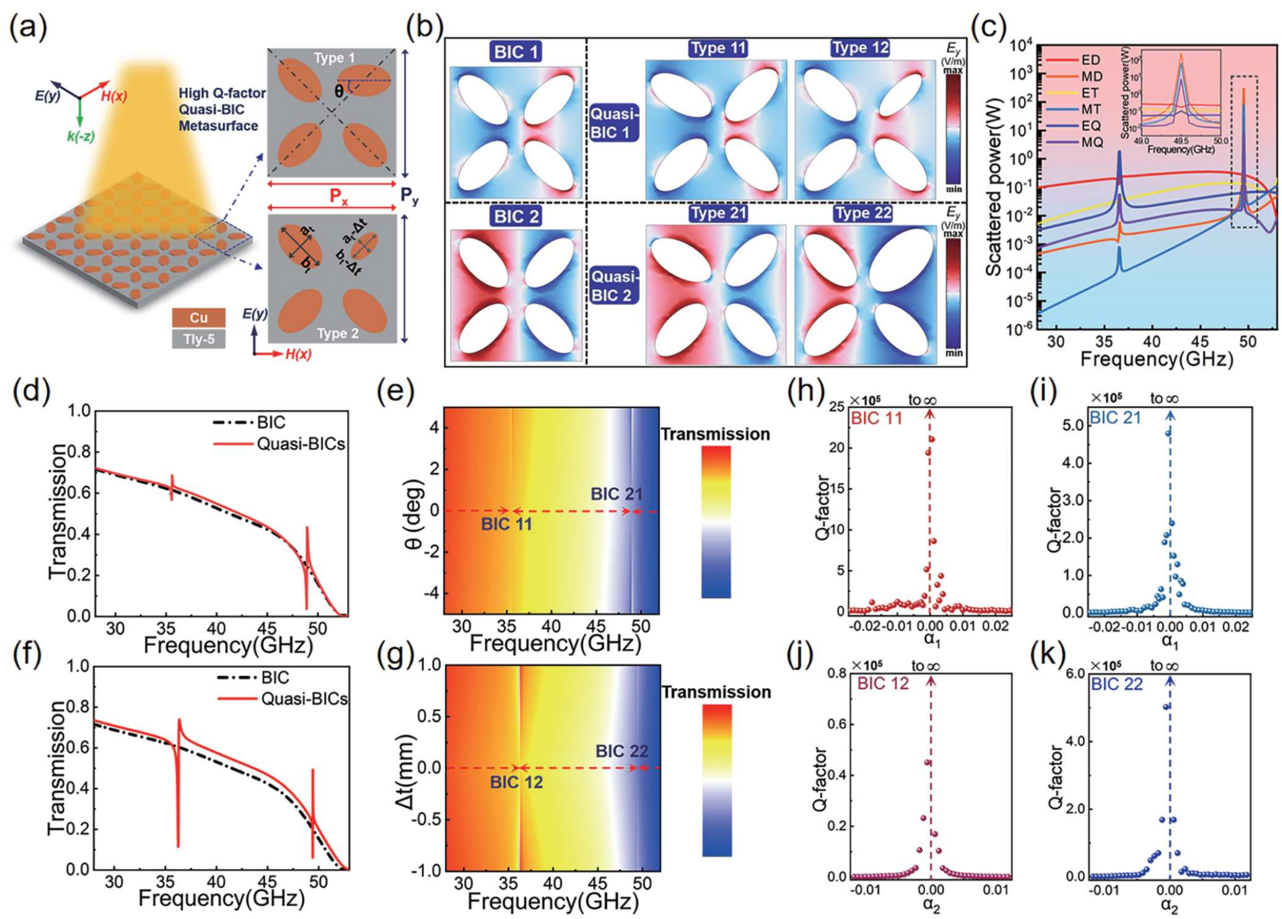

Figure 1 (Color online) Radiation leakage and dual quasi-BICs radiative coupling in a symmetry-protected BIC metasurface. (a) Schematic of a BIC optical metasurface comprising four symmetric elliptical Cu resonators on a Tly-5 substrate. p_x and p_y denote the lattice periods, and z indicates the wave-vector direction. Symmetry is deliberately broken by varying the ellipse size by Δt and by rotating the ellipses by an angle θ. (b) Calculated electric field profiles of the E_y component for the BIC and quasi-BIC modes in the x-y plane. Two types of structural asymmetrical perturbations (type 1m and Type 2m, where m=1, 2) are introduced to break the original symmetry of the metasurface. The BIC 1 and BIC 2 at the high-symmetry Γ point with ultrahigh Q-factors are two symmetry-protected BICs. (c) Scattered power (logarithmic scale) for the six major multipoles moments, including the ED, the MD, the ETD, the MTD, the EQD, and the MQD. (d)-(g) Simulated transmission spectra illustrating the BIC modes and the quasi-BIC modes with dual resonance windows. (e) and (g) show the evolution from the BIC modes to the quasi-BIC modes. The linewidth of the quasi-BIC resonances gradually broadens with increasing tuning parameters θ and Δt, while an ideal zero-linewidth BIC appears at the high-symmetry point. (h)-(k) Q-factors of the BIC modes vary with the degree of asymmetry. The asymmetry parameter: $\alpha_1=(S-\Delta S)/S$ (S=4p×$a_t\times b_t$, ΔS=4p×$(a_t-\Delta t)\times(b_t-\Delta t)$), $\alpha_2=\theta/180°$. Diverging at the high-symmetry point (asymmetry parameter $\alpha_1=\alpha_2=0$) and decreasing as the degree of symmetry breaking increases.

resonance windows at 36.2 and 48.4 GHz. Meanwhile, the resonance linewidths of quasi-BIC modes 1 and 2 broaden progressively with increasing structural asymmetry. As discussed in Supplementary Materials section 3, the polarization characteristics of the excitation light source or the incident angle critically modulate the coupling between the light field and the metasurface, leading to incomplete coupling between the metasurface radiation mode and far-field radiation, resulting in the appearance of quasi-BICs. Different types of BICs exhibit distinct electric field localization characteristics. The E_y field distributions reveal the spatial confinement features of both BIC and quasi-BIC modes, as shown in Figure 1(b). BIC and quasi-BIC modes can be systematically identified and verified via eigenfrequency simulations, multipole expansion, and experimental Q-factor analysis [57,58]; accordingly, multipole decomposition is adopted here for modal analysis of the proposed BIC system. The corresponding multipole scattering powers shown in Figure 1(c) indicate that BIC 1 is predominantly governed by the electric quadrupole (EQ), while BIC 2 is mainly dominated by the magnetic dipole (MD). When the structural symmetry is broken, weak dipole moments are activated, giving rise to finite far-field radiation and the formation of quasi-BIC modes with extremely narrow bandwidths. Furthermore, the two BIC modes considered here exhibit ultrahigh Q-factors, with the Q-factor of BIC 1 and BIC 2 reaching up to 2.10×10^6 and 2.02×10^5, respectively, as shown in Figure 1(h)-(k). The Q-factor decreases as the degree of symmetrical breaking increases. The ultrahigh Q-factors and low radiation losses of BIC metasurfaces offer an unprecedented approach for light-matter interaction, opening new opportunities for future communication systems.

2.2 Coupled-mode theory and parameter tuning

Symmetry breaking causes in-plane energy leakage of the BIC metasurface into free space, transforming the dark-state BIC modes into quasi-BIC modes with an ultra-narrow linewidth. The transmission spectra of BIC 1 and BIC 2 both exhibit sharp, asymmetric Fano line shapes. Thus, we theoretically analyze these two localized modes using coupled-mode theory (CMT) [59-62]. For the two-mode system, s_1 and s_2 denote the complex modal amplitudes, while S_n^{in} and S_n^{out} denotes the incident or outgoing wave energy of each mode (where the superscript "in" refers to the incident wave, "out" refers to the outgoing wave, and the subscripts "+" and "−" refer to the wave propagating in the positive and negative directions, respectively). γ_{in} and γ_{on} (n=1, 2) represent the internal and external loss coefficients associated with the nth modes, respectively. $m_{12}(m_{21})$ is the coupling coefficient between mode 1 and mode 2. Under temporal CMT, the coupled system can be expressed as follows [61,63-66]:

$$\begin{pmatrix}\gamma & 0\\ 0 & \gamma\end{pmatrix}\cdot\begin{pmatrix}s_1\\ s_2\end{pmatrix}=\begin{pmatrix}-\tau_{o1}^{-1/2} & 0\\ 0 & -\tau_{o2}^{-1/2}\end{pmatrix}\cdot\begin{pmatrix}S_{1+}^{\text{in}}+S_{1-}^{\text{in}}\\ S_{2+}^{\text{in}}+S_{2-}^{\text{in}}\end{pmatrix}, \tag{1}$$

here, $\gamma_{nn}=\mathrm{i}\omega-\mathrm{i}\omega_n-\gamma_{\text{in}}-\gamma_{\text{on}}$ (n=1, 2), $\gamma_{\text{on}}=\omega_n/(2Q_{\text{on}})$, and $\gamma_{\text{in}}=\omega_n/(2Q_{\text{in}})$. Where, ω_n is the resonant angular frequency, Q_{on} is the external loss quality factor of the n mode, and Q_{in} is the internal loss quality factor of the nth resonant mode, respectively. The relevant quality factors conform to the following equation: $1/Q_{\text{tn}}=1/Q_{\text{on}}+1/Q_{\text{in}}$. Here, Q_{tn} is the total quality factor of the n-th resonant mode, and its numerical value is obtained from the following formula: $Q_{\text{tn}}=f/\Delta f$ (f and Δf represent the resonance frequency and the half-power bandwidth of the nth mode in the system, respectively). In the present metasurface system, the two quasi-BICs modes originate from different multipolar resonances (EQ and MD) and exhibit negligible mutual coupling. Therefore, the cross-coupling coefficients μ_{12} and μ_{21} can be reasonably approximated as zero. Additionally, the numerical value of the internal loss quality factor can be calculated by dividing the real and imaginary parts of the effective refractive index. We can derive the transmission coefficient of this BIC metasurface system as follows: $t=\frac{S_{2+}^{\text{out}}}{S_{1+}^{\text{in}}}=\mathrm{e}^{i\varphi_1}-\tau_{o1}^{-1/2}\mathrm{e}^{i\varphi_1}A-\tau_{o2}^{-1/2}B$. Parameters A, B, and analytical derivations are shown in the Supplementary Materials section 1. Therefore, we can further calculate the transmission: $T=|t|^2$. By tuning the orientation (θ) and size (Δt) of the metallic ellipses, the intrinsic structural symmetry is deliberately broken, transforming the dark-state BIC mode in the transmission spectra into quasi-BIC modes characterized by dual resonance windows and ultranarrow linewidths. The theoretical fittings based on CMT exhibit excellent agreement with the numerical simulations, accurately capturing the optical response of the metasurface structure, as presented in Figure 2 (a) and (b).

Introducing in-plane perturbations can induce coupling between localized states and the radiation continuum, resulting in Quasi-BICs with ultrahigh Q-factors. Typically, these quasi-BIC modes exhibit minimal energy leakage, which is strongly dependent on the in-plane asymmetry of the metasurface and the coupling strength between adjacent resonators. In this structure, the size of the elliptical patches arranged in a plum-blossom pattern directly affects the coupling between the in-plane electric dipole and quadrupole. With the hs=0.762 mm and the long axis a_t=1.2 mm and in-plane symmetry broken (θ=5° and Δt=0.1 mm), tuning the minor semi-axis b_t from 0.4 to 0.8 mm introduces structural perturbations that reduce the phase velocity of the quasi-BIC mode, leading to a pronounced redshift of the resonance frequency, as shown in Figure 2(e) and (f). Within the main tuning range, the data exhibits an approximately linear dependence, as presented in Figure 2(g) and (h),

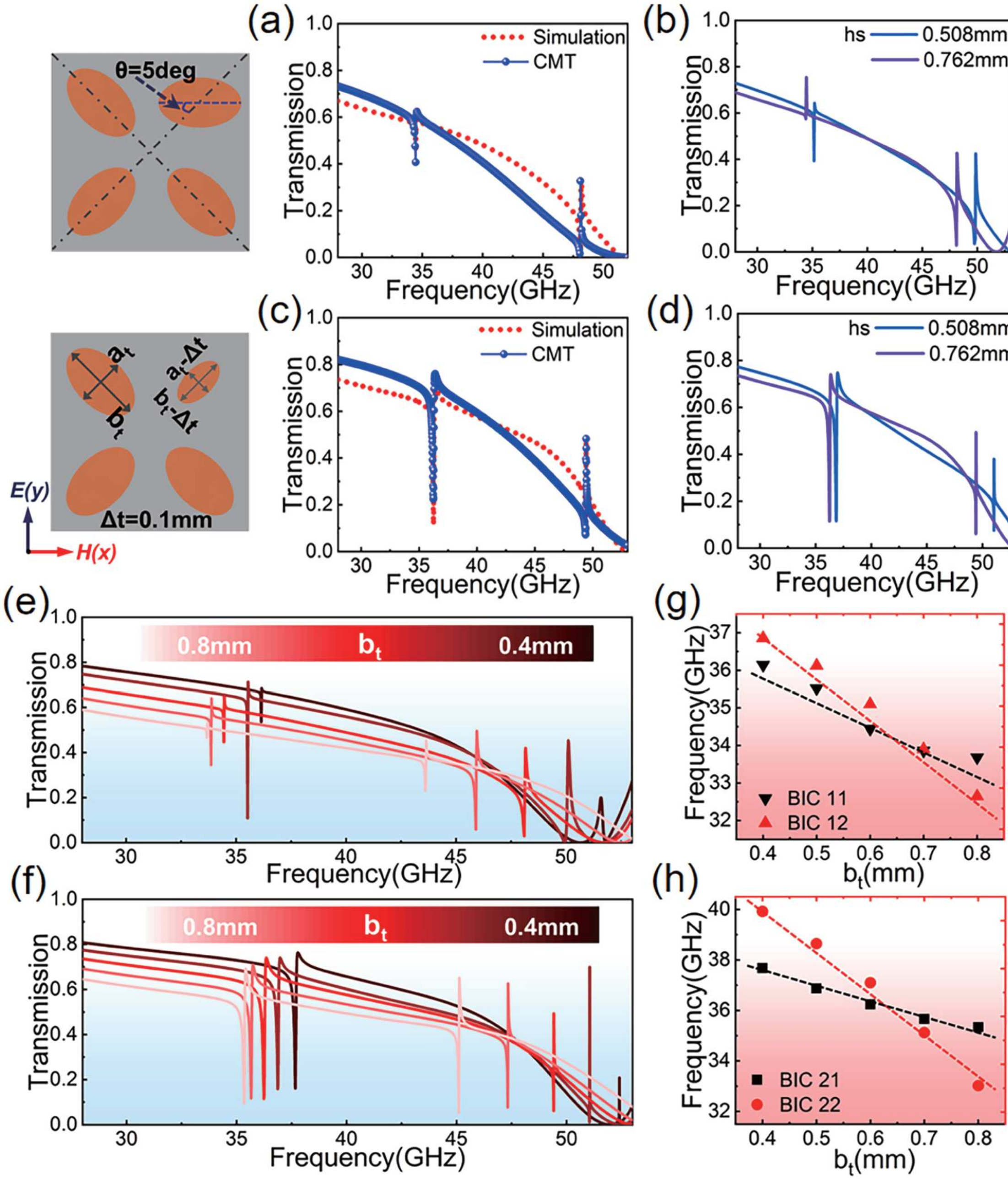

Figure 2 (Color online) Simulated and numerical transmission spectrum of quasi-BIC resonances under different symmetry-breaking configurations, together with the parameter tuning of the quasi-BICs metasurface. (a) and (c) Comparison between temporal CMT fits and full-wave simulations for quasi-BIC modes exhibiting two resonance windows. (b) and (d) Influence of the Tly-5 substrate thickness (hs) on the quasi-BIC transmission resonances. (e) and (f) A pronounced redshift is observed in the transmission spectrum of the quasi-BIC modes with dual resonance windows as the short semi-axis (b_t) of the metallic ellipse increases from 0.4 to 0.8 mm. (g) and (h) Redshift of the transmission-dip frequency with b_t, along with a linear fitting.

consistent with the first-order perturbative response of the quasi-BICs to symmetry breaking. Additionally, variations in the thickness of the dielectric substrate led to different levels of radiation loss. Increasing the thickness of the dielectric substrate raises the effective dielectric constant, resulting in a redshift of the resonance frequency for the quasi-BIC modes in the non-localized state, as shown in Figure 2(c) and (d). Details of the parameter tuning for the BIC metasurface at a substrate thickness of hs=0.508 mm can be found in the Supplementary Materials section 2. By tuning the geometric parameters, the resonant frequency of the quasi-BICs can be controlled, enabling potential applications in dynamic optical modulation, sensors, and optical guiding.

2.3 Aperture-coupled antenna with BIC metasurface

Owing to their momentum-space confinement, BIC modes can support non-radiative resonances with ultrahigh

Q-factors. By introducing structural perturbations, these modes can be coupled to external feeds, providing a low-loss mechanism for controlled radiation. Combined with aperture coupling, which isolates direct feed-radiator interaction and suppresses sidelobes and parasitic modes, this approach offers a promising route toward efficient, low-power 6G communication systems [55,56]. The proposed metasurface antenna is composed, from top to bottom, of a BIC metasurface radiating patch layer, a ground plane with coupling apertures, a dielectric support layer, and a feed layer, as shown in Figure 3(a). In the antenna design, a 4×4 metasurface array is utilized as a radiating patch and is aligned with the aperture center of the ground plane, thereby enhancing the radiation directivity and gain. Structural asymmetry is introduced through slight perturbations in the geometry to convert the symmetry-protected BIC into quasi-BIC modes, enabling controllable radiation leakage. The BIC metasurface patch layer is designed with geometrical parameters a_t=1.2 mm and b_t=0.3 mm, while the aperture of the ground layer is defined by: a_1=2 mm, a_2=a_3=2.5 mm, b_1=b_2=b_3=0.4 mm. Simulations are performed in CST using a frequency-domain solver, where periodic boundary conditions are applied along the *x*-direction and perfectly matched layers (PMLs) are imposed along the *y*-direction. A waveguide port is employed along the positive *z*-direction, normal to the structure. The metallic component (Cu) is modeled as lossless, whereas the dielectric substrate is Tly-5 with intrinsic loss, characterized by a complex relative permittivity of 2.2+0.0009i. The thickness of the layers is set to hs_1=hs_2=0.762 mm. By precisely tuning the aperture parameters, multiple operating modes can be excited within the target frequency band, leading to optimized impedance-matching characteristics. Compared with conventional patch-based radiating layers, the BIC metasurface exhibits superior impedance matching performance owing to its strong field localization and controllable radiation leakage characteristics. Consequently, the antenna exhibits an improved impedance bandwidth, as indicated by the S_{11} response in Figure 3(b). Furthermore, for aperture layers with different designs, the coupling and feeding efficiency with the BIC metasurface also vary, as shown in Figures 3(c)-(f). The antenna without any aperture exhibits poor overall impedance matching, with the S_{11} approaching −10 dB only at a few discrete frequencies. Introducing aperture structures significantly improves the impedance-matching performance across the desired frequency range. For the aperture 1 configuration, the operational band (S_{11}<−10 dB) is mainly distributed between 35 and 42 GHz, where multiple resonant points appear near 38 and 45 GHz, with a minimum return loss of −60.45 dB at 39.2 GHz. For the aperture 2 configuration, the operational bands extend from 30 to 35 GHz, with multiple resonances emerging at lower frequencies (25 and 27.5 GHz). When the two apertures are combined, the resulting coupling layer markedly enhances the antenna's impedance-matching capability, increasing the number of resonant frequencies and broadening the operational bandwidth. The minimum return loss reaches −50 dB at 33 GHz. The inclusion of the aperture layer not only effectively mitigates feed-induced coupling reflections and enhances the return-loss performance but also optimizes the coupling strength between the feed and the radiating elements. Consequently, the antenna exhibits improved ability to focus radiated energy and to control beam directionality.

On this basis, characteristic mode analysis is employed to evaluate the *Q*-factor of the designed metasurface antenna, where the total *Q*-factor is given by $1/Q_{\text{total}}=1/Q_{\text{rad}}+1/Q_{\text{loss}}$. Here, Q_{rad} characterizes radiation leakage, whereas Q_{loss} accounts for dissipative loss contributions such as conductor and dielectric losses. Owing to the adoption of a 4×4 BIC metasurface array as the radiating patch, the achievable Q_{total} cannot reach the ideal limit. For quasi-BIC metasurface patches with relatively high *Q*-factor ($Q\approx10^6$), sharper and deeper reflection coefficient notches are observed when coupled with different aperture configurations, indicating stronger energy confinement and higher frequency selectivity of the resonant modes, as shown by the red curves in Figure 3(g). In contrast, metasurfaces with lower *Q*-factor ($Q\approx10^2$) exhibit enhanced radiation leakage, resulting in broader resonance linewidths and smoother S_{11} responses with wider matching bandwidths. Such configurations demonstrate improved robustness with respect to different aperture designs, albeit at the expense of reduced matching depth at a single resonance frequency, as illustrated by the blue curves in Figure 3(g). Overall, these results highlight a fundamental trade-off in BIC-based metasurface antenna design: high-*Q* modes enable deep and highly selective impedance matching but suffer from narrow bandwidth and strong sensitivity to excitation conditions, whereas low-*Q* modes provide broader bandwidth and improved robustness at the expense of reduced matching depth. This trade-off offers a flexible design space for tailoring antenna performance according to specific application requirements.

2.4 Performance and experiment section

Table 1 compares our designed antenna with previously reported metasurface antennas. In contrast to earlier works, this study employs a BIC metasurface with high *Q*-factors as the radiating element, significantly reducing EM losses of the antenna. This enhancement improves the stability of the antenna at higher frequencies while also reducing its size. Combined with an aperture-coupled feeding mechanism, the antenna achieves a measured peak gain of 22.4 dBi, while its return-loss response is formed by the superposition of multiple resonant bands, resulting in an overall −10 dB operating coverage of 50.13% across 20-42 GHz. This

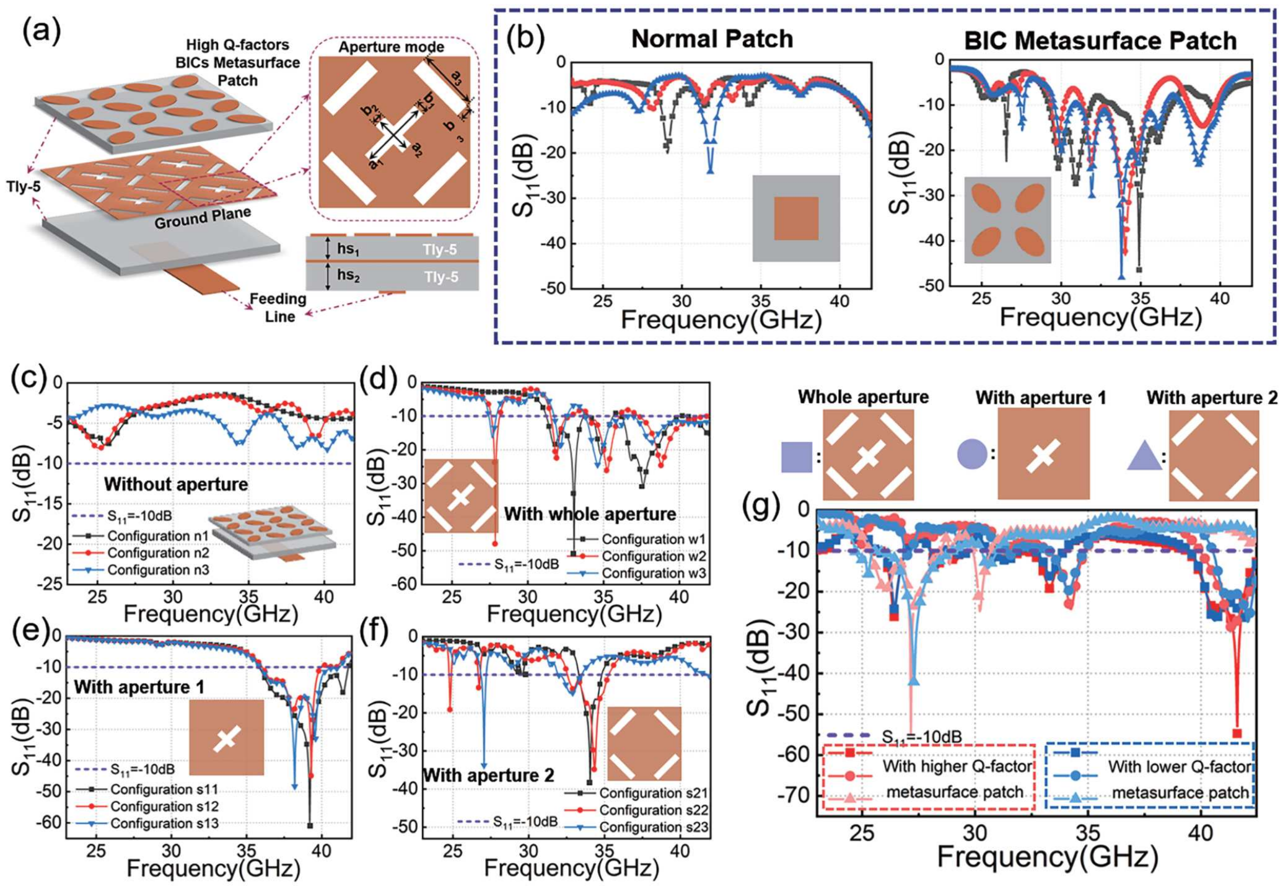

Figure 3 (Color online) Metasurface antenna architecture with high Q-factors BIC metasurface radiator and performance versus coupling apertures. (a) Exploded schematic illustrating the multilayer configuration from top to bottom: the BIC metasurface radiator, a slotted ground plane, and the feed layer. All dielectric substrates are Tly-5 with respective thicknesses of hs_1 and hs_2. The ground-plane coupling aperture is composed of two symmetrically arranged slots: a cross-shaped slot (aperture 1) and a rectangular slot (aperture 2). (b) A comparative test was conducted on the S_{11} performance of a conventional square radiating patch and a BIC metasurface radiating patch under the same aperture conditions. (c)-(f) Simulated S_{11} for metasurface antennas employing different aperture geometries. The −10 dB return-loss threshold (purple dashed line) defines the operational bandwidth, highlighting the influence of aperture geometry on resonant behavior. (g) Simulated S_{11} of antennas employing metasurface patches with different Q-factor resonances under distinct aperture geometries. The red solid line corresponds to higher Q-factor metasurfaces, whereas the blue solid line denotes lower Q-factor ones. The square, circle, and triangle markers indicate configurations with whole aperture, aperture 1, and aperture 2, respectively.

demonstrates an attractive combination of high gain and multi-resonance broadband performance. The fabrication process of the metasurface antenna, including the 4×4 unit cell antenna array, is illustrated in Figure 4(a). The detailed fabrication process is provided in the Supplementary Materials section 5. To validate the antenna's performance, we conducted experimental testing of the S_{11} parameter using a vector network analyzer and compared the results with simulation data. The antenna fabrication process, including copper-clad etching, cleaning, and the resulting antenna samples, as shown in Figure 4(b), with detailed model parameters provided in Table S1 from the Supplementary Materials section 4. The measured results for the antennas with configurations w1 and w2 are in good agreement with the simulated results in the range of 30-42 GHz, as presented in Figure 4(c). At lower frequencies (<30 GHz), deviations between simulation and measurement are likely caused by fabrication tolerances, finite-size effects, and slight variations in the aperture geometry and alignment, which shift the resonance frequencies toward lower values. The test results for antennas using Configuration s11 and Configuration s12 exhibit coupling resonance points at higher frequencies, while the test results for the antennas made with Configuration s21 and Configuration s22 show coupling resonance points at mid-to-low frequencies, consistent with the simulation results, as shown in Figure 4(d) and (e). However, the dip values of the S_{11} parameters in the test results are slightly lower than those in the simulation results. Without loss of generality, the preset positions of the radiating elements and apertures play a critical role in determining the antenna's impedance matching characteristics.

A similar trend can also be observed in the antenna gain. The antenna employing the full aperture exhibits better gain performance, reaching 22.4 dBi at 24.5 GHz, while aperture

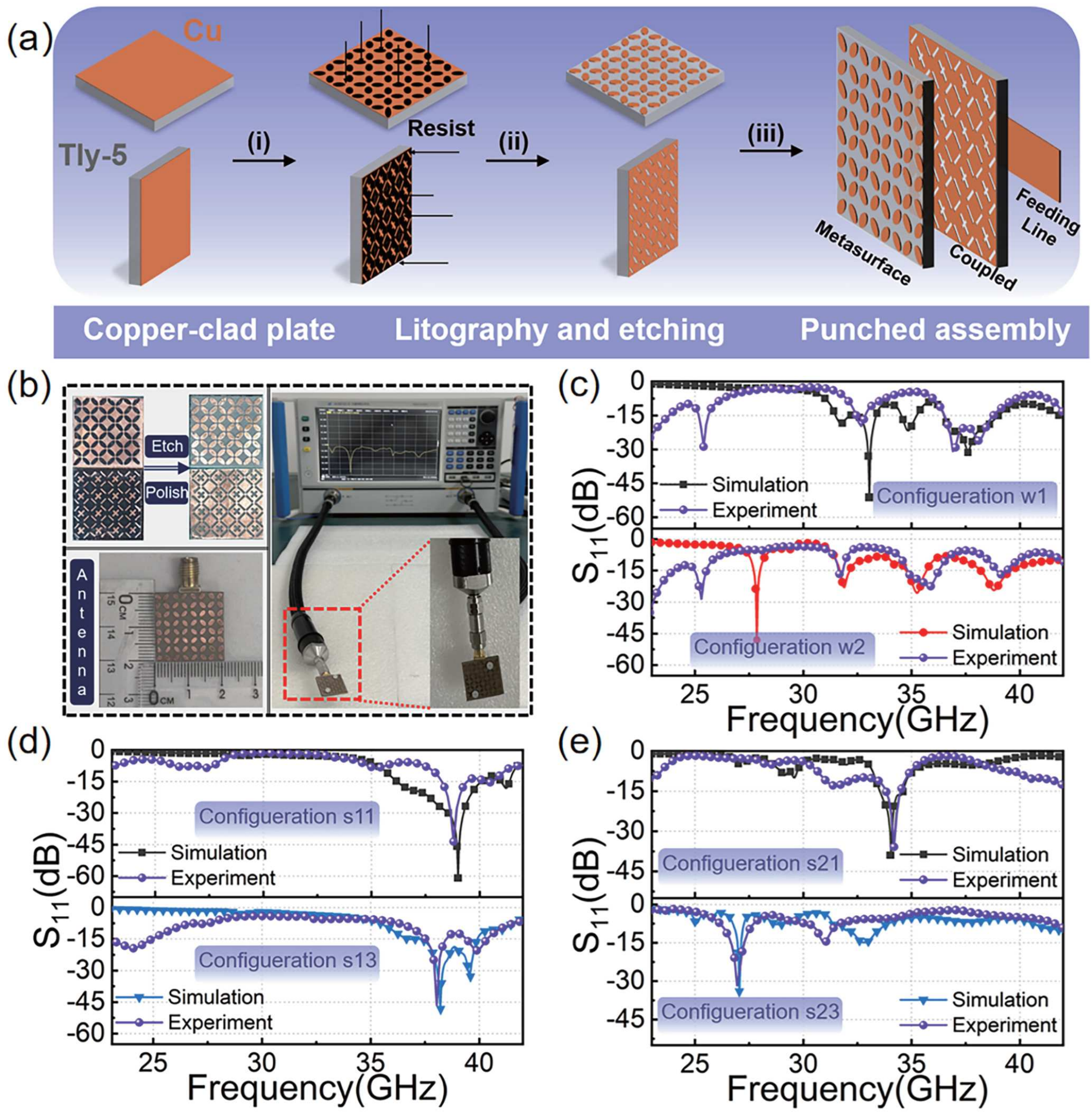

Figure 4 (Color online) Fabrication workflow and experimental characterization of the BIC metasurface antenna. (a) Fabrication workflow for the BIC metasurface antenna. (i) Thermal transfer of the designed pattern onto a Cu-clad Tly-5 substrate; (ii) wet etching of the exposed copper followed by polishing to define the pattern; (iii) assembly of the etched radiating layer with the slotted aperture layer. (b) Measurement setup using a vector network analyzer. Photographs show the Cu-clad board before and after etching, along with the port-connection scheme. The fabricated sample measures 20 mm×20 mm. (c)-(e) Comparison of measured and simulated reflection coefficients (S_{11}) for selected metasurface-antenna samples. The purple curves represent measurements, while the dark-gray, red, and blue curves correspond to full-wave simulations.

1 and aperture 2 show stable radiation enhancement over different frequency bands, as illustrated in Figure 5(b). The gain and radiation characteristics were further measured in an anechoic chamber, as shown in Figure 5(a). In the practical measurements, the maximum measured gain is 18.1 dBi due to fabrication-induced dimensional deviations and additional losses. Nevertheless, the overall gain remains relatively stable within the operating bands, as shown in Figure 5(c)-(e). Meanwhile, the normalized radiation patterns in Figure 5(f)-(h) indicate that the measured antenna maintains clear directional radiation characteristics in both the V-plane and H-plane, verifying that the antenna can achieve directional radiation with acceptable beam stability. However, the main-lobe shapes in the primary radiation region are not

Table 1 Comparison of the proposed metasurface antenna with other works

Ref.	Feeder type	Feeding method	Freq. (GHz)	Peak gain. (dBi)	Area. (cm^2)	Bandwidth. S-parameters (<−10 dB)
[66]	SIW-patch	SIW	35	18	0.8×0.8	11.6%
[67]	30GHz: Horn	Horn	26-39	15	346.0	43.1%
[68]	Metasurace patch	Microstrip	7-13	23.6	4.1×3.9	41.7%
[69]	Stack patch	Coaxial	20-30	24	42.3	53.7%
[70]	metasurace patch	Aperture-coupled	3-7	15	0.4×0.4	38.2%
This work	BICs metasurace patch	Aperture-coupled	20-42	22.4	0.2×0.2	Multiple resonant windows 50.13%

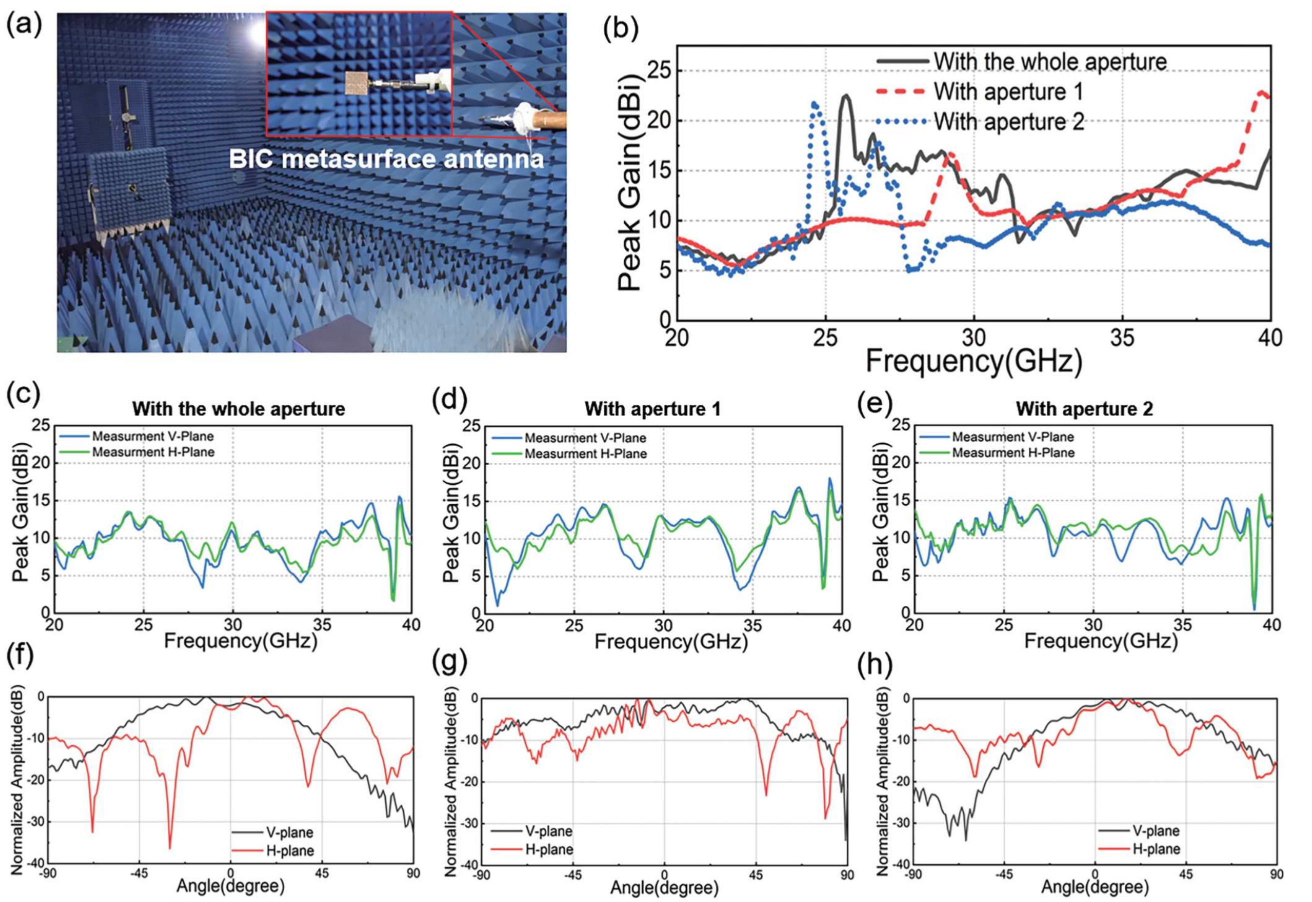

Figure 5 (Color online) Test setup and results of antenna gain and radiation patterns. (a) Measurement setup for radiation pattern measurement. (b) Simulated realized gain of BIC metasurface antennas incorporating different coupling apertures, accompanied by far-field radiation patterns at 25.7, 40.6, and 41.7 GHz, demonstrating geometry-dependent directivity evolution. (c)-(e) Measured gain performance of the antenna in the V- and H-planes with different apertures. (f)-(h) Normalized radiation patterns at 25.7 GHz with the whole aperture, at 29.6 GHz with aperture 1, and at 24.6 GHz with aperture 2.

entirely consistent, suggesting that the radiation patterns vary under different operating conditions and frequency points. This provides useful guidance for further optimization of the aperture-field distribution and coupling configuration. These results demonstrate that the proposed aperture-coupled BIC metasurface antenna can simultaneously realize broadband matching, high gain, and stable directional radiation, showing strong potential for extended millimeter-wave antenna applications.

3 Conclusion

In this work, we proposed an aperture-coupled metasurface antenna driven by BICs for extended millimeter-wave communications. By breaking the in-plane structural symmetry, the BIC mode is converted into a quasi-BIC mode with ultrahigh Q-factors, resulting in dual resonance windows with exceptionally narrow linewidths in the transmission spectrum, along with tunable linewidths and frequencies. The low-loss nature of this metasurface effectively suppresses EM dissipation, greatly enhancing radiation efficiency and enabling both high-gain and multi-band performance. Experimental verification using an aperture-coupled configuration confirms that the proposed metasurface antenna operates efficiently across the extended millimeter-wave band, achieving a maximum gain of 22.4 dBi, a return loss as low as −60.45 dB, and an overall bandwidth of 50.13%, enabled by the superposition of multiple resonant windows. Moreover, the impedance-matching characteristics can be further optimized by tailoring the aperture geometry, providing flexibility for diverse 6G deployment scenarios. In summary, the BICs concept mainly serves as a mechanism-oriented framework for understanding the resonant behavior of the metasurface, while the overall antenna performance is jointly determined by finite-size effects, aperture coupling, and multiple resonant contributions. This offers a promising pathway for the development of next-generation intelligent metasurface antennas for future 5G/6G communication systems.

This work was supported by the National Natural Science Foundation of China (Grant Nos. 62065017, 12004327, and 52303352), the Key Research and Development Program of Shaanxi Province (Grant No. 2024GX-YBXM-097), the Natural Science Foundation of Shaanxi Province (Grant No. 2021JM-414), and Scientific Research Projects of Yan'an University (Grant No. 2023CGZH-009).

Conflict of interest The authors declare that they have no conflict of interest.

Supporting Information

The supporting information is available online at http://phys.scichina.com and https://link.springer.com. The supporting materials are published as submitted, without typesetting or editing. The responsibility for scientific accuracy and content remains entirely with the authors.

1 M. Banafaa, I. Shayea, J. Din, M. Hadri Azmi, A. Alashbi, Y. Ibrahim Daradkeh, and A. Alhammadi, Alex. Eng. J. **64**, 245 (2023).
2 F. Tang, X. Chen, M. Zhao, and N. Kato, IEEE Wireless Commun. **30**, 72 (2023).
3 H. Yang, J. Xu, M. Peng, H. He, Y. Jiang, D. Yu, R. Jin, Y. Gu, Y. Hu, H. Duan, et al., Sci. Adv. **11**, eadz5123 (2025).
4 R. Chataut, M. Nankya, and R. Akl, Sensors **24**, 1888 (2024).
5 S. Dang, O. Amin, B. Shihada, and M. S. Alouini, Nat. Electron. **3**, 20 (2020).
6 M. Giordani, M. Polese, M. Mezzavilla, S. Rangan, and M. Zorzi, IEEE Commun. Mag. **58**, 55 (2020).
7 C. X. Wang, X. You, X. Gao, X. Zhu, Z. Li, C. Zhang, H. Wang, Y. Huang, Y. Chen, H. Haas, et al., IEEE Commun. Surv. Tutorials **25**, 905 (2023).
8 I. Tomkos, D. Klonidis, E. Pikasis, and S. Theodoridis, IT Prof. **22**, 34 (2020).
9 A. Dogra, R. K. Jha, and S. Jain, IEEE Access **9**, 67512 (2021).
10 L. H. Shen, K. T. Feng, and L. Hanzo, ACM Comput. Surv. **55**, 1 (2023).
11 V. K. Quy, A. Chehri, N. M. Quy, N. D. Han, and N. T. Ban, IEEE Access **11**, 39824 (2023).
12 Z. N. Chen, X. Qing, W. Liu, H. Sheng, T. Li, and B. Zhang, IEEE Commun. Mag. **62**, 94 (2024).
13 X. Wang, Y. Hou, J. Wang, Q. Chen, Y. Guo, Y. Yu, T. Zhou, L. Li, and Y. Wang, Opt. Express **33**, 31958 (2025).
14 M. El Badawe, T. S. Almoneef, and O. M. Ramahi, Sci. Rep. **6**, 19268 (2016).
15 G. Minatti, E. Martini, and S. Maci, IEEE Trans. Antennas Propagat. **65**, 1532 (2017).
16 G. B. Wu, J. Y. Dai, K. M. Shum, K. F. Chan, Q. Cheng, T. J. Cui, and C. H. Chan, Nat. Commun. **15**, 7202 (2024).
17 L. Hu, P. Jiang, H. Yang, Y. Qin, W. Caiyang, Y. Zheng, J. Deng, J. He, and J. Yang, Optics Commun. **526**, 128906 (2023).
18 X. Wang, Q. Chen, J. Wang, Y. Wang, Y. Hou, T. Zhou, Y. Guo, and B. Chen, Optics Lasers Eng. **197**, 109491 (2026).
19 J. Y. Dai, L. X. Yang, J. C. Ke, M. Z. Chen, W. Tang, X. Li, M. Chen, Z. H. Wu, Q. Cheng, S. Jin, et al., Laser Photonics Rev. **14**, 1900133 (2020).
20 N. Shlezinger, G. C. Alexandropoulos, M. F. Imani, Y. C. Eldar, and D. R. Smith, IEEE Wireless Commun. **28**, 106 (2021).
21 P. Dai, H. Chen, and W. Wang, Opto-Electron. Plus **1**, 250005 (2025).
22 M. De Carlo, S. Romano, F. Dell'Olio, and V. M. N. Passaro, Photon. Res. **14**, A39 (2026).
23 Y. Yi, Q. Song, L. Jiang, Z. Yi, Y. Yi, and M. Long, Optics Laser Tech. **183**, 112372 (2025).
24 F. Lei, S. Wang, L. Wu, K. Wen, J. Zhu, J. Yang, and Y. Qin, J. Appl. Phys. **139**, 053105 (2026).
25 H. S. Khaliq, and H. R. Kim, Laser Photonics Rev. **20**, e01883 (2026).
26 Y. Shao, Z. Su, H. He, X. Jing, Y. Liu, G. Geng, J. Li, Y. Wang, and L. Huang, Opt. Express **32**, 23268 (2024).
27 T. Yu, M. F. Zhou, G. T. Cao, Y. N. Zhang, Y. L. Ouyang, Y. Liu, Y. Dai, H. Liu, L. A. Bian, L. Y. Cui, et al., Sci. Sin.-Phys. Mech. Astron. **56**, 234211 (2026).
28 J. Hu, C. Xiong, W. Li, L. Liu, and S. Zhang, Sci. Sin.-Phys. Mech. Astron. **56**, 264212 (2026).
29 Y. J. Zang, R. H. Chai, W. Liu, Z. C. Li, H. Cheng, J. G. Tian, and S. Q, Chen, Sci. Sin.-Phys. Mech. Astron. **67**, 244212 (2024).
30 Z. Huang, J. Wang, W. Jia, S. Zhang, and C. Zhou, Appl. Phys. Lett. **125**, 141702 (2024).
31 P. Brugnolo, S. Arslanagic, and R. E. Jacobsen, Phys. Rev. Lett. **134**, 096902 (2025).
32 C. Damgaard-Carstensen, T. Yezekyan, M. L. Brongersma, and S. I. Bozhevolnyi, ACS Nano **19**, 11999 (2025).
33 S. Mohamed, J. Wang, H. Rekola, J. Heikkinen, B. Asamoah, L. Shi, and T. K. Hakala, Laser Photonics Rev. **16**, 2100574 (2022).
34 G. Xu, Z. Xue, J. Fan, D. Lu, H. Xing, P. P. Shum, Y. Zhou, and L. Cong, Adv. Mater. **36**, 2406526 (2024).
35 C. Zhou, L. Huang, R. Jin, L. Xu, G. Li, M. Rahmani, X. Chen, W. Lu, and A. E. Miroshnichenko, Laser Photonics Rev. **17**, 2200564 (2023).
36 J. Wang, J. Kühne, T. Karamanos, C. Rockstuhl, S. A. Maier, and A. Tittl, Adv. Funct. Mater. **31**, 2104652 (2021).
37 M. V. Gorkunov, A. A. Antonov, and Y. S. Kivshar, Phys. Rev. Lett. **125**, 093903 (2020).
38 Z. Li, G. Nie, J. Wang, F. Zhong, and S. Zhan, Phys. Rev. Appl. **21**, 034039 (2024).
39 X. Yan, M. Tang, Z. Zhou, L. Ma, Y. Vaynzof, J. Yao, H. Dong, and Y. S. Zhao, Nat. Commun. **16**, 2375 (2025).
40 M. Kang, M. Xiao, and C. T. Chan, Phys. Rev. Lett. **134**, 013805 (2025).
41 M. Kang, L. Mao, S. Zhang, M. Xiao, H. Xu, and C. T. Chan, Light Sci. Appl. **11**, 228 (2022).
42 Y. Chen, X. Yang, and J. Gao, Light Sci. Appl. **7**, 84 (2018).
43 Y. Chen, H. Deng, X. Sha, W. Chen, R. Wang, Y. H. Chen, D. Wu, J. Chu, Y. S. Kivshar, S. Xiao, et al., Nature **613**, 474 (2023).
44 Y. Chen, S. Qian, K. Wang, X. Xing, A. Wee, K. P. Loh, B. Wang, D. Wu, J. Chu, A. Alu, et al., Nat. Nanotechnol. **17**, 1178 (2022).
45 L. Huang, S. Li, C. Zhou, H. Zhong, S. You, L. Li, Y. Cheng, and A. E. Miroshnichenko, Adv. Funct. Mater. **34**, 2309982 (2024).
46 J. Ji, B. Zhou, P. Bøggild, S. Al-Daffaie, P. U. Jepsen, and J. Gomez Rivas, Adv. Photonics Res. **5**, 2400020 (2024).
47 W. Ma, and C. Zhou, Opt. Lett. **48**, 2158 (2023).

48 M. Kang, S. Zhang, M. Xiao, and H. Xu, Phys. Rev. Lett. **126**, 117402 (2021).
49 G. Sun, Y. Wang, Z. Cui, R. Xie, and X. Zhao, Appl. Phys. Lett. **124**, 111704 (2024).
50 D. R. Abujetas, J. Olmos-Trigo, and J. A. Sánchez-Gil, Adv. Opt. Mater. **10**, 2200301 (2022).
51 D. Zheng, and Y. S. Lin, Small Struct. **5**, 2300529 (2024).
52 Civerolo M., and Arakaki D. IEEE International Symposium on Antennas and Propagation (New York, IEEE, 2011), pp. 876–879.
53 S. Sahin, N. K. Nahar, and K. Sertel, J. Infrared Millim. Terahertz Waves **40**, 557 (2019).
54 I. F. Akyildiz, C. Han, and S. Nie, IEEE Commun. Mag. **56**, 102 (2018).
55 M. Luo, Y. Zhou, X. Zhao, Z. Guo, Y. Li, Q. Wang, J. Liu, W. Luo, Y. Shi, A. Q. Liu, et al., ACS Nano **18**, 6477 (2024).
56 C. Huang, L. Liang, P. Chang, H. Yao, X. Yan, Y. Zhang, and Y. Xie, Adv. Mater. **36**, 2310493 (2024).
57 G. Nousios, J. F. Algorri, W. Fuscaldo, F. Dell'Olio, S. Romano, G. Zito, B. Miranda, Y. Ding, V. Dmitriev, L. C. Andreani, et al., Optics Laser Tech. **192**, 113398 (2025).
58 J. F. Algorri, F. Dell'Olio, Y. Ding, F. Labbé, V. Dmitriev, J. M. López-Higuera, J. M. Sánchez-Pena, L. C. Andreani, M. Galli, and D. C. Zografopoulos, Optics Laser Tech. **161**, 109199 (2023).
59 A. Fu, C. Wang, S. Chen, K. Yang, B. Ren, and P. Chen, Opt. Express **32**, 41619 (2024).
60 W. Huang, S. Liu, Y. Cheng, J. Han, S. Yin, and W. Zhang, New J. Phys. **23**, 093017 (2021).
61 H. A. Haus, W. P. Huang, N. A. Whitaker, and S. Kawakami, J. Lightwave Technol. **5**, 16 (1987).
62 W. Huang, S. T. Cao, X. Qu, W. Zhang, S. Yin, and J. Han, IEEE Trans. Microwave Theor. Techn. **72**, 1520 (2024).
63 E. D. Denman, J. Math. Anal. Appl. **21**, 242 (1968).
64 H. Son, T. Choi, K. Kim, Y. Kim, J. Bang, S. J. Kim, B. Lee, and Y. Jeong, ACS Photonics **11**, 3221 (2024).
65 S. Fan, W. Suh, and J. D. Joannopoulos, J. Opt. Soc. Am. A **20**, 569 (2003).
66 R. Gao, M. Q. Yang, Q. Y. Guo, and W. He, IEEE Trans. Antennas Propagat. **72**, 6209 (2024).
67 S. Xu, Y. Shen, S. Xue, and S. Hu, IEEE Trans. Antennas Propagat. **71**, 8548 (2023).
68 F. Qin, Y. Liu, C. Gu, L. Zeng, W. Cheng, H. Zhang, and S. Gao, IEEE Trans. Antennas Propagat. **72**, 6992 (2024).
69 X. Liu, X. Wang, G. M. Yang, D. Xiang, and L. R. Zheng, Opt. Express **32**, 13851 (2024).
70 Q. Gu, X. Zheng, Y. Zhou, F. Sun, and S. Liu, IEEE Access **11**, 104858 (2023).